

SIMULATIONS OF SYNCHROTRON-RADIATION-INDUCED ELECTRON PRODUCTION IN THE CESR VACUUM CHAMBER WALL

J.A. Crittenden, S. Poprocki, D.L. Rubin and D. Sagan
CLASSE, Cornell University, Ithaca NY 14853

Abstract

We report on calculations of electron production by synchrotron radiation absorbed in the vacuum chamber walls of the Cornell Electron Storage Ring (CESR). These photoelectrons are the source of electron clouds which limit the performance of storage rings by causing betatron tune shifts, instabilities and emittance growth. Until now, cloud buildup modeling codes have used ad hoc models for the production of the seed electrons. We have employed the photon scattering code Synrad3D developed at Cornell University to quantify the pattern of absorbed photons around the CESR ring, including the distribution in azimuthal location on the wall of the beampipe. The reflectivity of the wall, including its dependence on photon incident angle and energy, is modeled for various materials using online look-up tables. Micro-groove structure in the vacuum chamber wall is also accounted for. The resulting absorbed photon energy and incident angle information are used as input to Geant4-based simulations of electron emission from the walls, in which the material composition of the wall is also taken into account. The quantum efficiency is found to vary dramatically with the location of the absorption site, owing to the distribution in photon impact energies and angles. The electron production energy spectrum plays an important role in the modeling of electron cloud buildup, where the interplay of production energy and acceleration by the beam bunches determines the time structure and multipacting characteristics of the cloud.

INTRODUCTION

The buildup of high densities of low-energy electrons has been recognized as an important operational limitation in a variety of accelerator facilities since the 1960s [1]. In positron storage rings such as KEKB and the Cornell Electron Storage Ring (CESR), as well as in the proton rings at the Large Hadron Collider, a primary source of electron production is synchrotron-radiation-induced photon absorption processes in the vacuum chamber walls. Thus the incident photon rate and quantum efficiency for producing electrons are critical factors in the time dependence of the electron densities and their interaction with the beam bunches. The quantum efficiency depends strongly on the wall material and surface properties, as well as on the incident photon energy and angle. The photon absorption rates, energies, and angles of incidence determine the azimuthal electron production locations on the vacuum wall surface around the ring, and in the various magnetic field environments, on which the subsequent evolution of the cloud depends. In addition, the cloud dynamics depend crucially on the photoelectron production energies, since, together with the

momentum kicks imparted by the beam bunches, they determine the cloud density profile present at the arrival time of succeeding bunches.

Joining a multi-decade collaborative effort, the CESR Test Accelerator (CESRTA) project [2] has undertaken a series of measurements, both local and ring-wide, to quantify, characterize and model the buildup of electron clouds, with the goal of extending the predictive power of the models to include betatron tune shifts and emittance growth and contributing to the robust design of future accelerator facilities. Recent experimental and modeling work on tune shifts increasing along a train of positron bunches has motivated the present study of photoelectron production in the CESR vacuum chamber walls throughout the entire circumference of the ring.

This paper first describes recent improvements in the photon tracking simulation. The physics of reflection from grooved surfaces and thin surface layers has been incorporated. We then present the results of the Geant4 code used to generate 10^5 events in each of 720 bins in transverse azimuthal photon absorption site location on the vacuum chamber wall, using samples of individual photon energies and incident angles collected from the photon tracking summed over the field-free and dipole regions of the ring. In the following, we refer to the electrons produced inside the beampipe volume via photoelectric effect and atomic de-excitation processes as photoelectrons. We show as well the dependence on vacuum chamber wall material used as input to the Geant4 simulation. The CESR vacuum chamber wall material is modeled as 3 mm of aluminum 6061 alloy with a 5-nm layer of CO, a choice consistent with reflectivity measurements of material samples in X-ray beams [3]. These Geant4 simulations provide the electron production rate in units of electrons per meter per beam particle per radian in the 720 bins around the transverse perimeter of the beampipe separately for the field-free and dipole regions of the ring. The electron production energy spectrum from 1 eV to 5 keV is provided separately in three regions of azimuthal production location, again separately for the field-free and dipole regions. These distributions in electron production location and energy are provided to the cloud buildup code, which uses them in separate simulations for the field-free and dipole cases, as described in Refs. [4, 5].

The results presented below concern primarily modeling for a 5.3 GeV positron beam, with a summary of results for the 2.1 GeV and 6.0 GeV modeling included in tabular form for comparison.

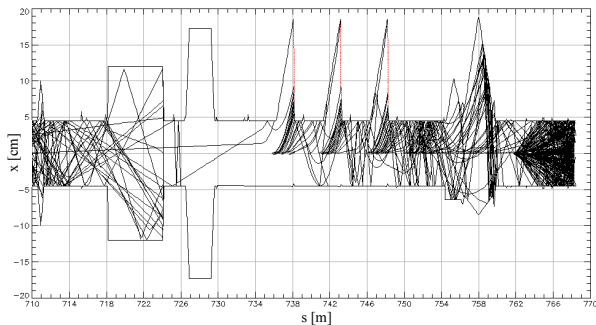


Figure 1: Top down view (x vs. s) for a portion of the CESR ring, showing photon tracks (black lines). The red vertical lines represent X-ray beam line exit ports, and any photon hitting those surfaces is terminated and excluded from the absorbed photon rate.

SYNCHROTRON RADIATION PHOTON TRACKING CALCULATION

An essential tool in this study is the photon-tracking calculation Synrad3D [6]. It provides for the generation of individual photons radiated by the positron beam, and incorporates a user-defined 3D model of the vacuum chamber to model the reflection and absorption of photons using the Bmad library [7] and X-ray data from an LBNL database [8]. Figure 1 shows a plan view of photon trajectories in a region of the CESR ring which includes X-ray beamline exit windows at which incident photons are not included in the tally of electron-producing photon strikes.

Photon reflectivity plays a crucial role in electron cloud buildup, since it determines the distribution of photon absorption sites around the ring. Absent photon reflectivity, few photons could be absorbed on the top and bottom of the beampipe, where photoelectron production is the primary source of cloud generation in the vertical plane containing the beam.

A micro-groove structure on the surface of the vacuum chamber, arising from the beampipe extrusion process, has been measured using atomic force microscopy and studied in X-ray beams as well [3]. These grooves are roughly parallel to the beam axis and understood to be caused by the beampipe extrusion process. Their effect is taken into account separately from the 100-nm surface roughness used in the diffuse scattering in Synrad3D, by incorporating the groove structure into the beampipe model. Figure 2 shows a diagram of the modeled grooves used in the photon-tracking simulation, and Fig. 3 shows the effect of the grooves on the photon tracks.

Figure 4 shows the result of the enhancement in larger reflection angles. The absorbed photon rate on the top and bottom of the beampipe increases by a factor of about three.

The reflectivity is also critically dependent on the material composition of the vacuum chamber wall. Figure 5 shows the fraction of photons reflected as a function of photon energy for a 5° grazing angle for aluminum with or without

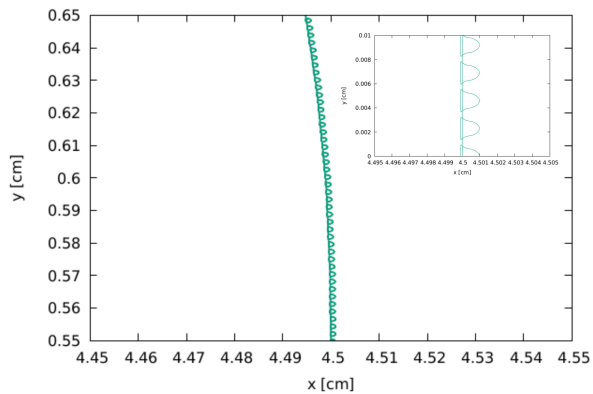


Figure 2: Schematic diagram of the 10-micron grooves on the CESR vacuum chamber wall used in the photon reflectivity model.

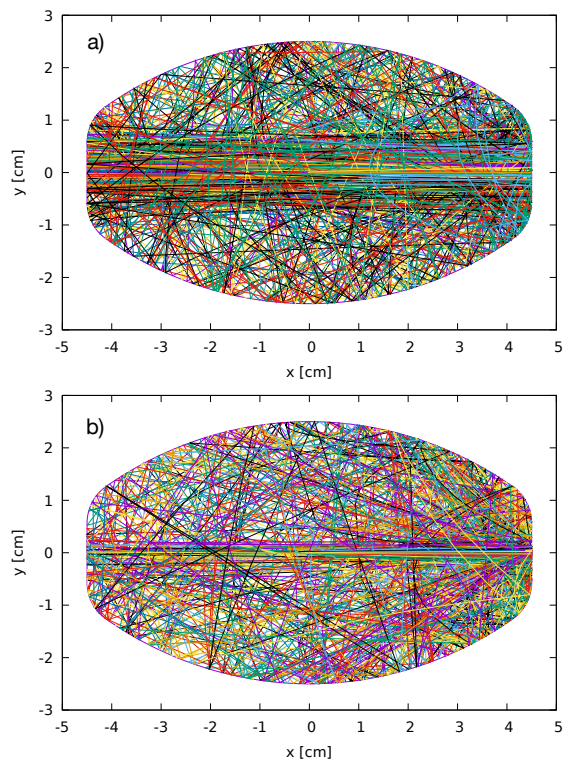


Figure 3: Photon tracking a) without and b) with grooves. The groove pattern results in greatly enhanced scattering out of the horizontal mid-plane. The apparent curvature in the tracks is a consequence of the longitudinal bend in the reference trajectory in the dipole.

C and CO surface layers. In validating our modeling studies, we have chosen to use the 5-nm CO layer, as in Ref. [3].

The photon tracking simulation identifies 10^6 locations around the CESR ring where photons are absorbed, along with the energy and incident angle of the photon. Figure 6 shows the linear density of absorption sites around the 768-m-circumference CESR ring, as well as the energy distribution of the absorbed photons and the number of reflections prior to absorption.

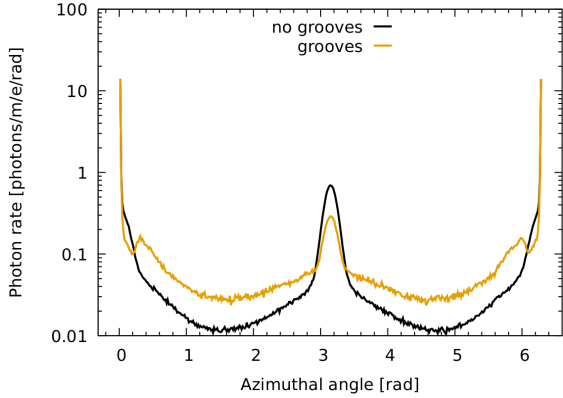


Figure 4: Comparison of the azimuthal absorption location of the absorbed photons when the micro-grooves are introduced in the CESR vacuum chamber geometry. The azimuthal angle is defined to be 180° in the midplane on the inside of the ring.

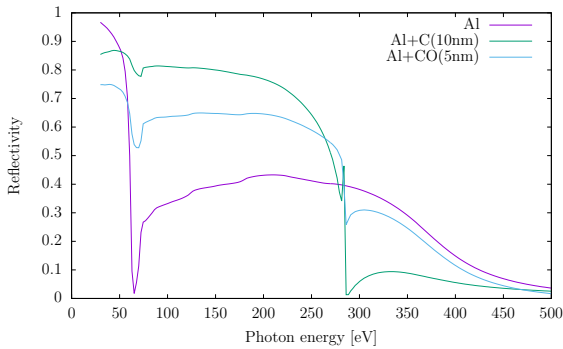


Figure 5: Smooth-surface photon reflectivity versus photon energy for aluminum, aluminum with a 10-nm carbon layer, and aluminum with a 5-nm carbon monoxide layer, for photons incident at a 5° grazing angle. The data were obtained from the LBNL database [8].

Only reflected photons strike the top, bottom and inner walls of the vacuum chamber. The typical number of reflections before absorption depends on the transverse azimuthal Φ_{180} angle of the absorption site location, where Φ_{180} ranges from -180° to $+180^\circ$ with its origin in the mid-plane on the outside of the ring. Figure 7 a) shows the dependence of the average number of reflections prior to absorption on this angle. Figure 7 b) shows the average number of prior reflections of the photons absorbed on the outer wall of the chamber. Figures 7 c), d) and e) show the distributions in the number of prior reflections for the azimuthal ranges $|\Phi_{180}| < 1.5^\circ$, $1.5 < |\Phi_{180}| < 165^\circ$, and $|\Phi_{180}| > 165^\circ$, respectively. For $|\Phi_{180}| < 1.5^\circ$, 83% of the photons were not reflected prior to absorption.

Due to the correlation of azimuthal angle with number of reflections, and the energy dependence of the photon reflectivity, we anticipate a correlation of photon energy with azimuthal angle. The dependence of absorbed photon energy on azimuth is shown in detail in Fig. 8. And since the probability for electron emission depends on photon energy,

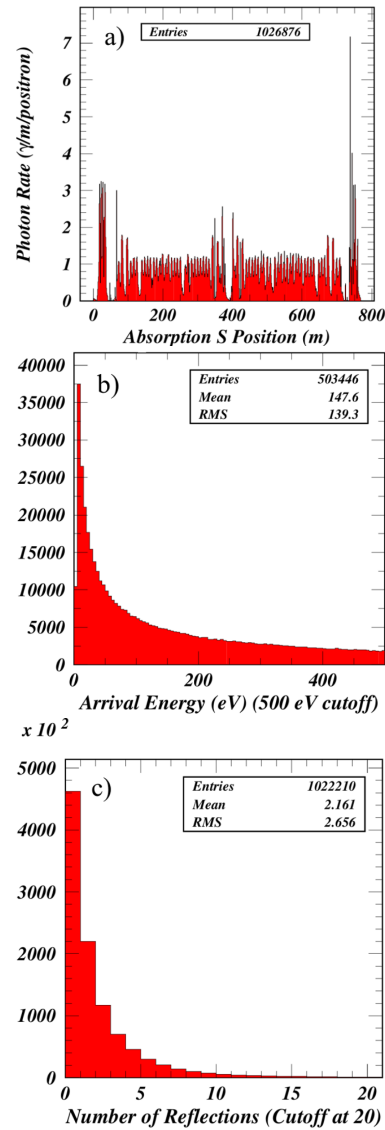


Figure 6: Distributions of absorbed photons in a) location along the CESR ring, b) photon energy and c) number of prior reflections.

we find that the effective quantum efficiency can depend strongly on azimuthal angle.

Figures 8 d), e), and f) illustrate the reasoning for choosing three distinct azimuthal regions when providing electron production energy distributions to the electron cloud buildup simulation. The average energy of the absorbed photons in the azimuthal ranges $|\Phi_{180}| < 1.5^\circ$, $1.5^\circ < |\Phi_{180}| < 165^\circ$ and $|\Phi_{180}| > 165^\circ$ is 2987 eV, 195 eV and 343 eV, respectively, averaged over the full ring.

We will see below in the section on the Geant4 simulations that the photoelectron production energy depends strongly on the angle of incidence of the photon on the chamber wall. Figures 9 and 10 show details of the photon angle distributions as functions of azimuthal impact location, summed over the field-free and dipole regions of the ring, respectively. The distributions in photon angle of incidence on

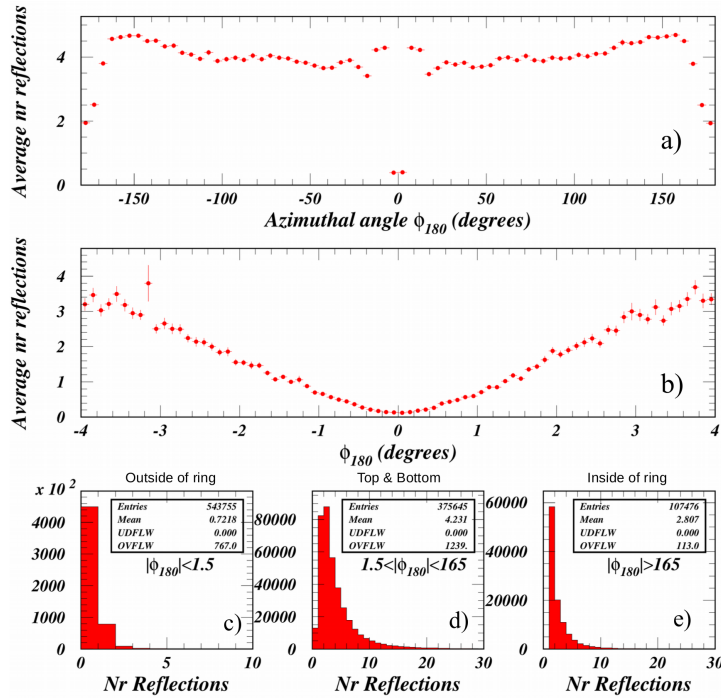


Figure 7: Average number of prior reflections for absorbed photons summed over the full ring a) as a function of the azimuthal location on the vacuum chamber wall, Φ_{180} , b) in the narrow range $\Phi_{180} < 4^\circ$. The distribution in the number of reflections are shown for the three azimuthal regions c) $|\Phi_{180}| < 1.5^\circ$, d) $1.5 < |\Phi_{180}| < 165^\circ$, and e) $|\Phi_{180}| > 165^\circ$.

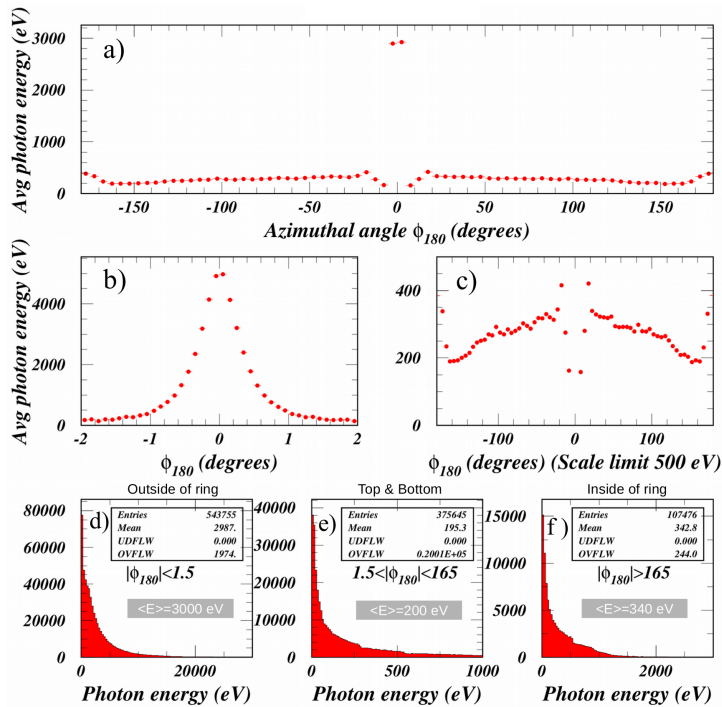


Figure 8: Average energy of the absorbed photons summed over the full ring a) as a function of the azimuthal location on the vacuum chamber wall, Φ_{180} , b) in the narrow range $\Phi_{180} < 2^\circ$, a region rich in unreflected photons, and c) the full azimuthal range, but with the vertical scale limited to a maximum of 500 eV in order to show details of the energy distribution for multiply reflected photons. The photon energy distributions are also shown for the three azimuthal regions for which electron energy distribution were provided to the electron cloud buildup simulation: d) $|\Phi_{180}| < 1.5^\circ$, d) $1.5 < |\Phi_{180}| < 165^\circ$, and f) $|\Phi_{180}| > 165^\circ$.

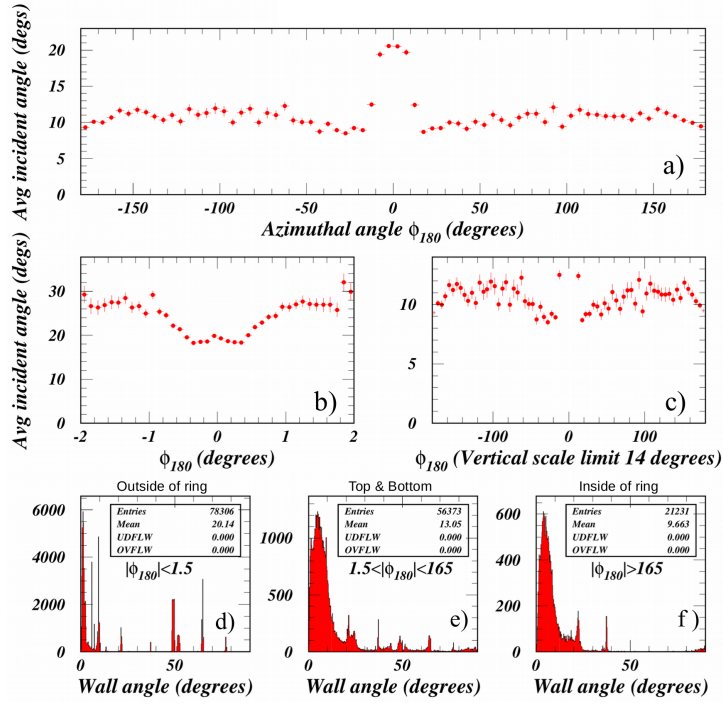


Figure 9: Average angle of incidence $\langle \theta_{\gamma}^{\text{inc}} \rangle$ of the absorbed photons summed over the field-free regions of the CESR ring a) as a function of the azimuthal location on the vacuum chamber wall, Φ_{180} , b) in the narrow range $\Phi_{180} < 2^\circ$, and c) the full azimuthal range, but with the vertical scale limited to a maximum of 14° in order to show details of the angular distribution for multiply reflected photons. These distributions are also shown for the three azimuthal regions c) $|\Phi_{180}| < 1.5^\circ$, d) $1.5 < |\Phi_{180}| < 165^\circ$, and f) $|\Phi_{180}| > 165^\circ$.

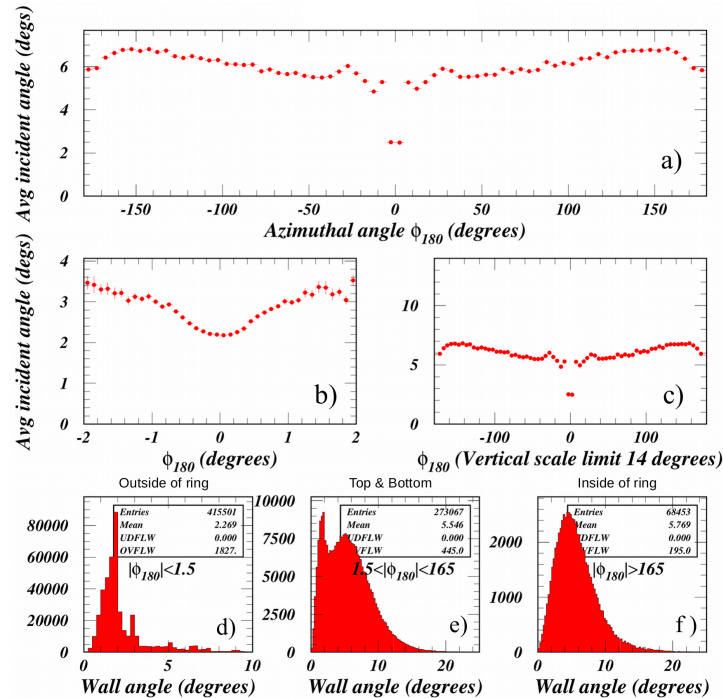


Figure 10: Average angle of incidence $\langle \theta_{\gamma}^{\text{inc}} \rangle$ of the absorbed photons summed over the dipole regions of the CESR ring a) as a function of the azimuthal location on the vacuum chamber wall, Φ_{180} , b) in the narrow range $\Phi_{180} < 2^\circ$, and c) the full azimuthal range, but with the vertical scale limited to a maximum of 14° in order to show details of the angular distribution for multiply reflected photons. These distributions are also shown for the three azimuthal regions c) $|\Phi_{180}| < 1.5^\circ$, d) $1.5 < |\Phi_{180}| < 165^\circ$, and f) $|\Phi_{180}| > 165^\circ$.

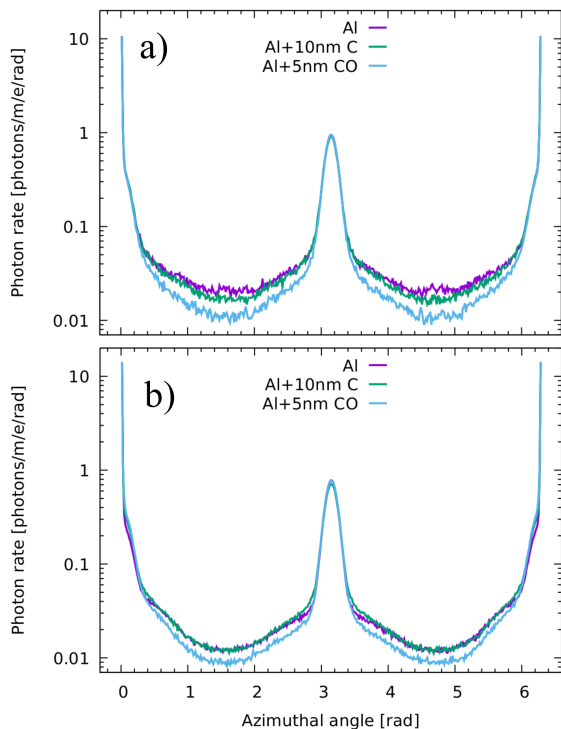


Figure 11: Azimuthal distribution of photon absorption rate averaged over a) field-free and b) dipole regions of the CESR ring.

the vacuum chamber wall are very different for dipole and field-free regions, with dramatic consequences for the average quantum efficiency. Generally the photons absorbed in the field-free regions have been multiply reflected and are of lower energy, which enhances the quantum efficiency. However, details of the vacuum chambers, such as gate valves, sliding joints and exit windows result in a complicated pattern of photon incident angles around the ring.

The photon tracking simulation thus provides the longitudinal and transverse location, and incident angle and energy on a photon-by-photon basis. Figure 11 shows the distribution in transverse azimuthal location of absorbed photons, averaged separately over the field-free and dipole regions of the ring.

GEANT4 SIMULATION RESULTS

Significant progress in simulating low-energy electromagnetic processes has been achieved over the past decade in the Geant4 simulations toolkit [9, 10], including both photoeffect and atomic de-excitation processes in a wide variety of materials [11].

Quantum efficiency

In order to determine the azimuthal dependence of the quantum efficiency, we subdivide the vacuum chamber wall into 720 azimuthal bins. The distribution of photons absorbed in each bin is determined by the photon tracking code. Given a sample of photon energies and angles of

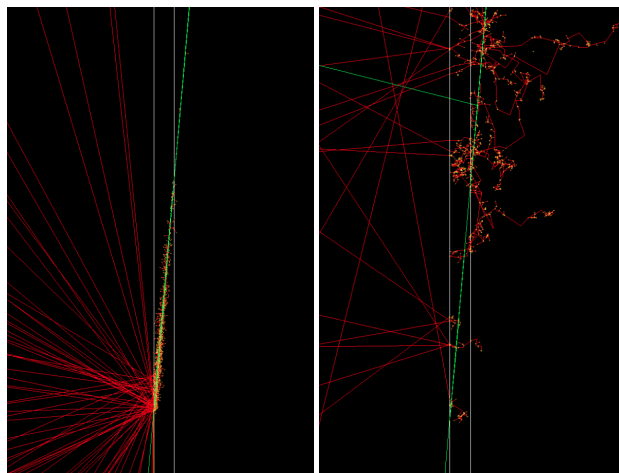


Figure 12: Tracks from incident photons (green), initially traveling left to right, and subsequently generated electrons (red) in the Geant4 simulation for photon energies of 30 eV (left) and 2 keV (right). Low-energy photons interact primarily with the 5-nm CO layer, while the higher energy photons interact in the aluminum. Electrons produced by photoeffect reach the interior of the vacuum chamber via rescattering, while those produced radially symmetrically by atomic de-excitation processes can exit the wall more directly.

incidence, the Geant4 code is used to generate 10^5 photoabsorption events, determining the rate of emitted electrons summed over the bin. Examples of such events are shown in Fig. 12.

We thus obtain a value for the electron production rate specific to the photon incident angle and energy distribution in each azimuthal bin, including (relatively rare) multi-electron production events. Figure 13 shows the detail with which Geant4 calculates average electron production rates for various wall materials.

The dependence of the quantum efficiency on the incident angle of the absorbed photon is very strong in the Geant4 modeling, as illustrated in Fig. 14, favoring more grazing angles. We recall that the average incident angle of the absorbed photons in the azimuthal ranges $|\Phi_{180}| < 1.5^\circ$, $1.5^\circ < |\Phi_{180}| < 165^\circ$ and $|\Phi_{180}| > 165^\circ$ is 20.14° , 9.66° , and 13.05° (2.27° , 5.77° , and 5.55°), in the field-free (dipole) regions, respectively.

Figure 15 shows azimuthal distributions in average quantum efficiency obtained from the Geant4 simulations for the 5.3 GeV positron beam. The resulting distributions in electron production rate in the 720 azimuthal bins provided to the electron cloud buildup simulation code for the case of the aluminum chamber with the 5-nm CO layer are shown in Fig. 16. The integrated rates are 0.0454 and 0.0839 electrons/m/positron for the field-free and dipole regions, respectively. Prior to this work, these two quantities and two values for effective average reflectivity around the ring served as input to the cloud buildup simulations.

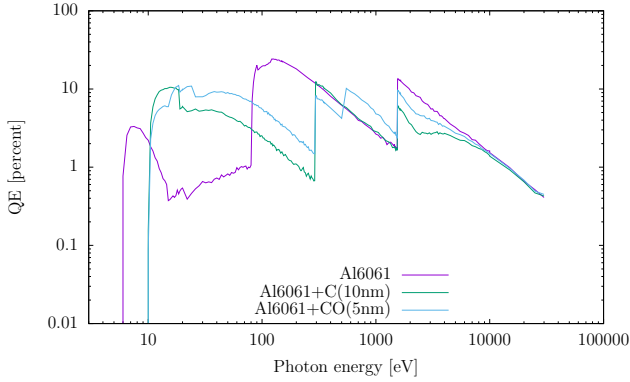


Figure 13: Quantum efficiency versus photon energy for photons incident at a 5-degree grazing angle, for the aluminum alloy 6061, aluminum with carbon layer, and aluminum with carbon monoxide layer. The quantum efficiency is sharply enhanced at photon energies above various atomic shell transition energies, such as aluminum L_{II} and L_{III} (73 eV), carbon K (284 eV), oxygen K (543 eV), and aluminum K (1560 eV).

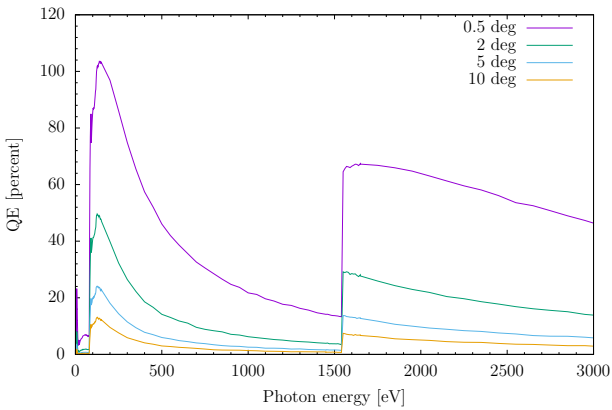


Figure 14: Quantum efficiency versus photon energy for photons incident at grazing angles between 0.5° and 10° for the aluminum alloy 6061 as modeled in Geant4.

Photoelectron energy distributions

In addition to the determination of quantum efficiencies, we obtain energy distributions of the photoelectrons in each of the three azimuthal regions $|\Phi_{180}| < 1.5^\circ$, $1.5 < |\Phi_{180}| < 165^\circ$ and $|\Phi_{180}| > 165^\circ$ by simulating 10^6 events in each region, again using absorbed photons from the photon tracking code. These distributions are shown for the CESR dipole regions in Fig. 17. Within each of these three angular regions, electron energy distribution is roughly independent of azimuthal angle. The quantum efficiency values and photoelectron energy distributions are obtained separately for the field-free and dipole regions of the ring, so a total of 1.5×10^8 simulated events are obtained for use in the electron cloud buildup simulations.

The simulation results for the photoelectron energy distributions show substantial high-energy tails, resulting in an average energy in the azimuthal ranges $|\Phi_{180}| < 1.5^\circ$,

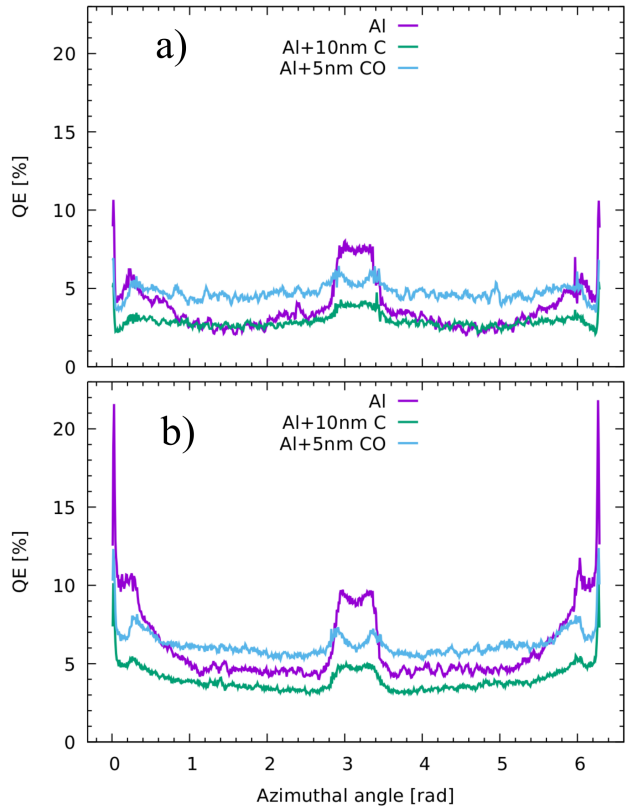


Figure 15: Azimuthal dependence of quantum efficiency for a) field-free regions and b) dipole regions of the CESR ring for aluminum and aluminum with a carbon or carbon monoxide layer.

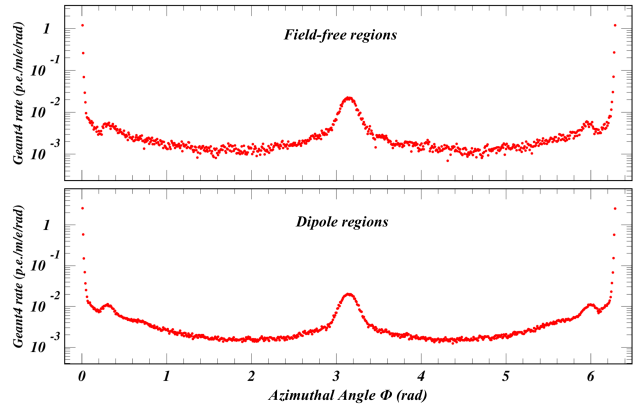


Figure 16: Electron production rates as a function of azimuthal production location on the vacuum chamber wall for a) field-free regions and b) dipole regions in units of electrons/m/positron/radian.

$1.5 < |\Phi_{180}| < 165^\circ$ and $|\Phi_{180}| > 165^\circ$ of 761 eV, 99 eV and 120 eV (662 eV, 78 eV and 110 eV), for the field-free (dipole) regions, respectively. These three energy distributions, as well as the average electron production rates in 0.5 degree azimuthal bins are provided separately for the field-free and dipole regions of the CESR ring as input to the electron cloud buildup calculations described in [4]. Our modeling has shown that it is important and, to an accu-

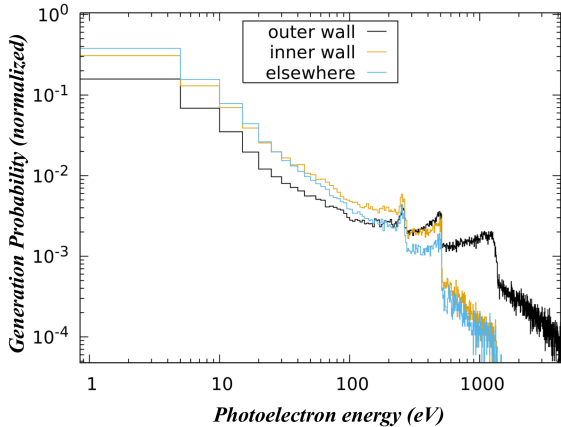


Figure 17: Electron energy distributions for production locations on the outside wall, inside wall, and elsewhere along the vacuum chamber summed over the dipole regions. Since lower energy photons are more likely to be reflected, the inner wall and elsewhere (including top & bottom) are struck by lower energy photoelectrons than is the outer wall at the midplane. These distributions are used as input to the electron cloud build-up simulations [4].

racy acceptable for comparing to measurements, sufficient to differentiate between the field-free and dipole-occupied regions, comprising 17% and 66% of the ring, respectively. The contribution to the simulated tune shift values from the remaining 17% of the ring are at the level of a percent.

The electron production energy distribution is of particular importance, since the dependence of, for example, betatron tune shifts varies dramatically, with beam bunch population between 0.6×10^{10} and 9.5×10^{10} positrons/bunch. The associated beam kicks for electrons produced at the wall can be comparable to the electron production energies. These Geant4 simulations show that the primary sources of high-energy electrons (>100 eV) are atomic de-excitation

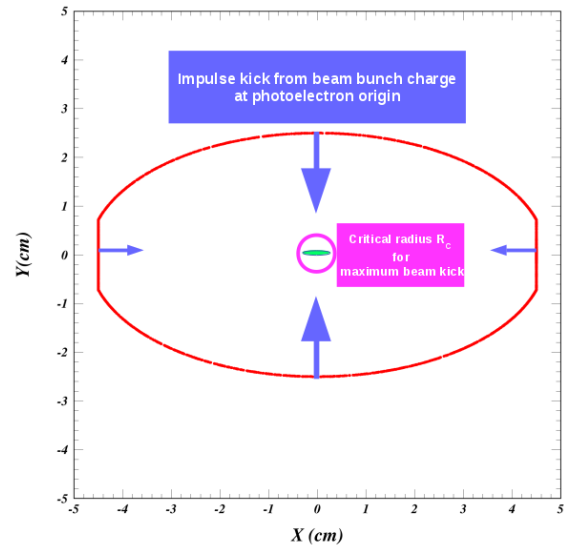


Figure 18: Schematic diagram of the laterally truncated elliptical CESR vacuum chamber illustrating the beam kicks for an electron produced at the wall and the radius R_C at which an electron receives the maximum kick.

processes, such as the Auger effect. The contribution of such electrons to cloud development is greater at lower bunch population, since their kinetic energies provide for higher subsequent secondary yields, replacing the effect of strong momentum kicks from the beam bunches. Figure 18 shows a schematic diagram of the CESR vacuum chamber illustrating the beam kick quantities in Table 1. In an impulse approximation, the beam bunch charge integrated over the bunch passage gives a momentum kick to an electron produced at the wall [13]. An electron generated simultaneously with the passage of the longitudinal center of the bunch, for example, receives half of this kick. We present the kick as the kinetic energy gained by the electron during the bunch passage. The elliptical shape of the vacuum chamber results

Table 1: Parameters for the acceleration provided by a positron bunch to a cloud electron located at the vacuum chamber wall on the X or Y axes. These examples correspond to the CESR-TA measurements of betatron tune shifts [4] as well as for the predictions for the 6.0 GeV upgrade of CESR [5, 12]. The total kick values are given as the kinetic energy of the electron following acceleration by the positron bunch in the impulse approximation. The direct and image kick values are signed according to whether they add or subtract from the total kick.

Beam energy (GeV)		2.085		5.289			6.000
Beam size $\sigma_X \times \sigma_Y \times \sigma_Z$ (mm)		0.735 \times 0.030 \times 9.2		1.44 \times 0.139 \times 15.8			1.44 \times 0.139 \times 15.8
Bunch population (10^{10})		0.64	1.12	3.25	6.66	9.54	3.52
Critical radius R_C (mm)		0.73	0.96	2.14	3.1	3.7	2.2
Maximum kick (keV)		1.2	2.5	3.5	9.0	14.1	3.9
$X=4.5$ $Y=0$ cm	Direct kick (eV)	0.16	0.5	41.8	17.6	36	4.9
	Image kick (eV)	-0.14	-0.44	-41.3	-15.6	-32	-4.3
	Total kick (eV)	0.02	0.06	0.5	2.0	4	0.6
$X=0$ $Y=2.5$ cm	Direct kick (eV)	0.50	1.6	13.4	56	115	15.8
	Image kick (eV)	0.60	1.6	13.9	59	120	16.3
	Total kick (eV)	1.10	3.2	27.3	115	235	32.1

an increased (reduced) kick in the vertical (horizontal) plane from the image charges ensuring the boundary conditions at the wall. The transverse beam size determines the critical radius R_C at which a cloud electron receives the maximum kick during bunch passage. Table 1 shows these values for the bunch populations and beam sizes for which CESR-TA betatron tune shift measurements are available, and also for the parameters of the upgraded Cornell High Energy Synchrotron Source to be commissioned at 6 GeV in 2019 [14]. Since the time interval between bunch passages is 14 ns, the kick corresponding to the horizontal (vertical) wall-to-wall traversal prior to the arrival of the succeeding bunch is 36 eV (9 eV). Another relevant consideration in this regard is that the secondary yield curve is maximum for an electron at perpendicular incidence carrying an energy of about 300 eV.

The wide range of beam kick values causes a great variation in the cloud dynamics as a function of bunch population and transverse beam size as evidenced in the patterns of tune shifts observed along a train of positron bunches [4]. The interplay between these kicks and the electron production energy distribution is an important aspect of the cloud buildup modeling.

Summary table

Table 2 compares the results of the photon tracking and photoelectron generation simulations for the 2.1, 5.3, and 6.0 GeV CESR lattices.

SUMMARY

We have implemented a Geant4-based post-processor for the Synrad3D photon-tracking code in order to obtain accurate values for the dependence of quantum efficiency on production location and a realistic photoelectron energy spectrum. We find that the quantum efficiency and electron production kinematics depend strongly on the vacuum chamber wall characteristics as well as on the location of photon absorption sites around the ring and on the incident photon grazing angles and energies. The coding tools provided by this work can be generalized to a wide variety of accelerators and vacuum chamber geometries and materials. For example, an initial study of the 97-km-circumference Future Circular Collider operating at 45.6 GeV with a NEG-coated copper chamber finds high quantum efficiencies (typically 20%, but reaching 70% in some regions) due to the small grazing angles of the photon wall strikes. More work is needed to assess quantitatively the effectiveness of the antechambers and the photon stops. The results of this study can be used to provide important input to electron cloud buildup modeling codes used at a wide variety of accelerators for purposes of understanding phenomena including betatron tune shifts, emittance growth, RF phase shifts, heat loads, and various types of instabilities.

ACKNOWLEDGMENTS

We thank E. Belli for useful information on the Future Circular Collider and K. Oide for making the FCC lattice

available. We also wish to acknowledge important contributions from the technical staffs of the Wilson Laboratory. This work is supported by National Science Foundation and by the US Department of Energy under contract numbers PHY-0734867, PHY-1002467 and DE-FC02-08ER41538 and DE-SC0006505.

Table 2: Results from the photon tracking and photoelectron generation simulations for the CESR-TA tune shift measurements at 2.1 and 5.3 GeV and for the 6.0 GeV CESR upgrade, where the new combined-function (C-F) magnet and undulator regions are modeled separately in addition to the field-free and dipole regions.

Beam energy (GeV)	2.085				
	Entire ring	Field-free	Dipole	C-F magnet	Undulator
Ring fraction (%)		16.5	65.6		
Number of photons	1064932	171987	710002		
Photon absorption rate ($\gamma/m/e+$)	0.765	0.378	0.370		
Number of electrons		3653092	4536786		
Electron production rate (p.e./m/e+)		0.02137	0.03144		
$\langle\theta_\gamma^{\text{inc}}\rangle$ on outside of ring (eV)	3.02	24.4	2.71		
$\langle\theta_\gamma^{\text{inc}}\rangle$ on top and bottom (eV)	5.99	12.26	5.59		
$\langle\theta_\gamma^{\text{inc}}\rangle$ on inside of ring (eV)	6.08	10.55	6.32		
$\langle E_\gamma \rangle$ on outside of ring (eV)	1443	867	1434		
$\langle E_\gamma \rangle$ on top and bottom (eV)	132	121	121		
$\langle E_\gamma \rangle$ on inside of ring (eV)	297	319	202		
$\langle E_{\text{electron}} \rangle$ on outside of ring (eV)		416	331		
$\langle E_{\text{electron}} \rangle$ on top and bottom (eV)		118	110		
$\langle E_{\text{electron}} \rangle$ on inside of ring (eV)		352	115		

Beam energy (GeV)	5.289				
	Entire ring	Field-free	Dipole	C-F magnet	Undulator
Ring fraction (%)		16.5	65.6		
Number of photons	1026876	155910	757021		
Photon absorption rate ($\gamma/m/e+$)	1.604	0.728	0.876		
Number of electrons		3740767	4552831		
Electron production rate (p.e./m/e+)		0.0454	0.0839		
$\langle\theta_\gamma^{\text{inc}}\rangle$ on outside of ring (eV)	2.40	20.14	2.27		
$\langle\theta_\gamma^{\text{inc}}\rangle$ on top and bottom (eV)	6.18	9.66	5.77		
$\langle\theta_\gamma^{\text{inc}}\rangle$ on inside of ring (eV)	5.93	13.05	5.55		
$\langle E_\gamma \rangle$ on outside of ring (eV)	2987	3079	2929		
$\langle E_\gamma \rangle$ on top and bottom (eV)	195	172	198		
$\langle E_\gamma \rangle$ on inside of ring (eV)	343	340	342		
$\langle E_{\text{electron}} \rangle$ on outside of ring (eV)		761	662		
$\langle E_{\text{electron}} \rangle$ on top and bottom (eV)		99	78		
$\langle E_{\text{electron}} \rangle$ on inside of ring (eV)		120	110		

Beam energy (GeV)	6.000				
	Entire ring	Field-free	Dipole	C-F magnet	Undulator
Ring fraction (%)		60.4	16.7	3.7	2.9
Number of photons	5006978	764360	3264221	336558	78187
Photon absorption rate ($\gamma/m/e+$)	3.77	0.833	0.973	1.655	0.3076
Number of electrons		3881357	4583462	4650963	4493193
Electron production rate (p.e./m/e+)		0.0603	0.0956	0.1241	0.0317
$\langle\theta_\gamma^{\text{inc}}\rangle$ on outside of ring (eV)	2.10	11.91	2.00	2.32	1.08
$\langle\theta_\gamma^{\text{inc}}\rangle$ on top and bottom (eV)	5.85	11.55	5.50	4.05	6.17
$\langle\theta_\gamma^{\text{inc}}\rangle$ on inside of ring (eV)	6.00	8.46	5.62	5.99	5.40
$\langle E_\gamma \rangle$ on outside of ring (eV)	3961	4346	3506	5949	7867
$\langle E_\gamma \rangle$ on top and bottom (eV)	200	174	206	181	151
$\langle E_\gamma \rangle$ on inside of ring (eV)	388	376	365	434	526
$\langle E_{\text{electron}} \rangle$ on outside of ring (eV)		889	747	809	1291
$\langle E_{\text{electron}} \rangle$ on top and bottom (eV)		108	86	287	218
$\langle E_{\text{electron}} \rangle$ on inside of ring (eV)		136	115	168	187

REFERENCES

- [1] F. Zimmermann, “Electron-Cloud Effects in Past & Future Machines—Walk through 50 Years of Electron-Cloud Studies,” in *Proceedings of E CLOUD 2012: Joint INFN-CERN-EuCARD-AccNet Workshop on Electron-Cloud Effects, La Biodola, Elba, Italy*, R. Cimino, G. Rumolo & F. Zimmermann, Eds., CERN, Geneva, Switzerland (2013), CERN-2013-002, p. 9–17.
- [2] “The CESR Test Accelerator Electron Cloud Research Program: Phase I Report,” Tech. Rep. CLNS-12-2084, LEPP, Cornell University, Ithaca, NY (Jan. 2013).
- [3] G. F. Dugan *et al.*, “Measurements of X-Ray Scattering from Accelerator Vacuum Chamber Surfaces, and Comparison with an Analytical Model,” *Phys. Rev. ST Accel. Beams* **18**, 040704 (Apr. 2015).
- [4] S. Poprocki *et al.*, “Measurements and simulations of electron-cloud-induced tune shifts and emittance growth at CESR-TA,” in *Proceedings of E CLOUD 2018: Joint INFN-CERN-EuroCirCol-ARIES-APEC Workshop on Electron-Cloud Effects, La Biodola, Elba, Italy*.
- [5] K. Rowan, “Revised Stability Predictions for CHES-U due to Electron-Cloud-Based Tune Shifts,” Tech. rep.
- [6] G. Dugan & D. Sagan, “Simulating synchrotron radiation in accelerators including diffuse and specular reflections,” *Phys. Rev. Accel. Beams* **20**, 020708 (Feb. 2017).
- [7] D. Sagan, “Bmad: A Relativistic Charged Particle Simulation Library,” *Nucl. Instrum. Methods Phys. Res.* **A558**, p. 356–359 (Mar. 2006).
- [8] B. L. Henke, E. M. Gullikson & J. C. Davis, “X-Ray Interactions: Photoabsorption, Scattering, Transmission, and Reflection at $E = 50\text{--}30,000$ eV, $Z = 1\text{--}92$,” *At. Data Nucl. Data Tables* **54**, p. 181–342 (Jul. 1993).
- [9] S. Agostinelli *et al.*, “Geant4—a simulation toolkit,” *Nuclear Instruments and Methods in Physics Research Section A: Accelerators, Spectrometers, Detectors and Associated Equipment* **506**, p. 250 – 303 (2003).
- [10] J. Allison *et al.*, “Recent developments in Geant4,” *Nuclear Instruments and Methods in Physics Research Section A: Accelerators, Spectrometers, Detectors and Associated Equipment* **835**, p. 186 – 225 (2016).
- [11] S. Incerti *et al.*, “Simulation of Auger electron emission from nanometer-size gold targets using the Geant4 Monte Carlo simulation toolkit,” *Nuclear Instruments and Methods in Physics Research Section B: Beam Interactions with Materials and Atoms* **372**, p. 91 – 101 (2016).
- [12] J. Crittenden *et al.*, “Electron Cloud Simulations for the Low-Emittance Upgrade at the Cornell Electron Storage Ring,” in *NAPAC2016: Proceedings of the North American Particle Accelerator Conference, Chicago, IL* (2016), Paper TUPOB23.
- [13] J. S. Berg, “Energy Gain in an Electron Cloud During the Passage of a Bunch,” LHC Project Report 97 (Jul. 1997), <https://cds.cern.ch/record/692004/files/project-note-97.pdf>.
- [14] J. Shanks *et al.*, “Accelerator Design for the CHES-U Upgrade,” (Oct. 2018), <https://arxiv.org/abs/1810.06557>.